Combining composition graded positive and negative electrodes for higher performance Li-ion batteries

Chuan Cheng,[a,b,*] Ross Drummond,[c] Stephen R. Duncan,[c] and Patrick S. Grant[a]

[a]Department of Materials, University of Oxford, Oxford OX1 3PH, UK.

[b]WMG, University of Warwick, Coventry CV4 7AL, UK.

[c]Department of Engineering Science, University of Oxford, Oxford OX1 3PJ, UK.

[*]Corresponding author, E-mail address: Chuan.Cheng@warwick.ac.uk (C. Cheng)

Abstract

Homogeneous electrode structures used in Li-ion batteries (LIB) lead to inhomogeneous active material utilization and gradients of overpotential and Li-ion concentration at the cell-scale, which are detrimental for both capacity retention at high charge-discharge rates and for battery life-time. To account for these gradients, we demonstrate that heterogenous electrode structures with engineered gradients in material distribution can improve LIB C-rate and long-term cycling performance when compared with conventional uniform electrodes in $LiFePO_4$ || $Li_4Ti_5O_{12}$ full-cell LIBs. An improvement in C-rate performance of > 120% and a capacity degradation rate reduced to <50% over uniform electrode cells was achieved at 1C, and graded cells showed a dramatically improved power-energy density balance. Graded electrodes had a relatively low cell polarization that became more marked as the C rate increased. Cycled graded electrodes had reduced solid electrolyte interphase (SEI) formation when compared with uniform electrodes according to XPS surface analysis, which was consistent with their reduced charge transfer resistance measured by impedance spectroscopy. The origin of the improved performance arises from a more uniform overpotential distribution across the thickness of the graded hetero-electrodes.

Graphical abstract

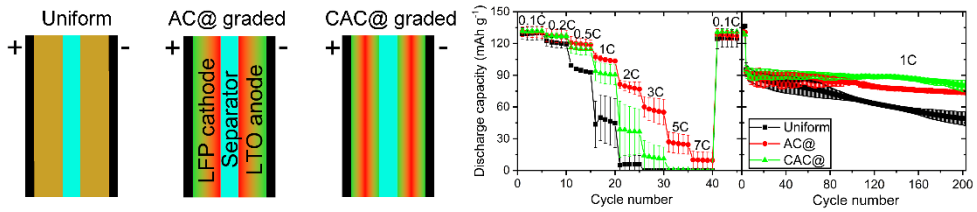

Keywords: Graded electrodes; Layer-by-layer spray deposition; Lithium-ion battery; Electrode engineering; Solid electrolyte interphase

1. Introduction

Li-ion battery (LIB) electrodes comprise the electrochemically active material, electrical conducting enhancer (usually carbon based) and a polymetric binder [1]. Optimization of electrode performance occurs by trial-and-error iteration to identify the best fraction of each constituent [2], alongside optimization of electrode thickness [3], pore fraction and exploitation of any opportunity to control directional pore distribution [4-8], porosity grading [2, 6, 9], and layering of constituents [10, 11]. These optimizations can significantly improve battery performance in terms of ion transport kinetics [3, 12], cell-scale energy density [2], degradation [13], or ohmic heat generation [14, 15], which are critical issues for practical applications such as electric vehicles [16-18].

The typical LIB electrode structure is isotropic at the macro-scale, comprising a homogenous mixture of constituents including active materials, carbon conductive additives, polymetric binders, and randomly distributed inter-connected porosity [19, 20]. However, due to restricted ion mobility in the tortuous pore structure [21, 22], the location of the current collectors, and anisotropic electric-field distribution when in operation, the Li-ion concentration and activation overpotential are inevitably inhomogenous through the electrode [23], especially at high charge-discharge rates when through-thickness or in-plane local ion concentration and overpotential gradients become more steep [24]. As a result, the electrochemically active material is inhomogeneously utilized in the critical energy storage reactions. For instance, neutron diffraction studies of a commercial LIB pouch cell showed that active material was mainly activated in the centre of the 2D electrode plane, while active material at the edges and far away from the current collector tabs was almost entirely inactive [25], resulting in capacity reduction at increased C-rate and inhomogeneous local degradation. This situation was similar for both cathode and anode [25], and is a generic issue not related to any particular

material. Similarly, through the electrode thickness, X-ray photoelectron spectra (XPS) surface analysis of cycled electrodes has shown that surface side-reactions leading to solid electrolyte interphase (SEI) formation were more extensive at the outer electrode surface near the separator compared with close to the current collector, which arose from inhomogeneous overpotential and reaction rates through the electrode thickness [26-28].

Thus, inhomogeneous material activation and spatially varying reaction rate induced by homogeneous electrode structures are inefficient and have detrimental effects on battery performance and lifetime, local capacity degradation, overheating and stress concentration [13]. This is an electrode-scale problem in LIBs, regardless of the specific electrode materials [29, 30].

The principal approach to improve (or homogenise) active materials utilization in LIB electrodes has been to reduce the pore tortuosity and/or to increase the pore fraction – both of which improve ion mobility and capacity at increasing charge/discharge rates. However, both approaches can have disadvantages, such as a decrease in overall volumetric capacity and/or difficulties in scaling the sacrificial pore template methods used for tortuosity control. These studies have shown that local porosity manipulation can be effective in improving overall active material utilization, but may not be the only approach to improving electrode performance for a given cell chemistry.

In this paper we investigate an alternative hypothesis: can changing (specifically, spatially grading) the local conductive carbon concentration in an electrode make a positive difference to electrode and full cell performance? We expect that changing the local conductive carbon fraction may change the local electronic conductivity (and resistance), and thus may have a direct, homogenizing effect on the local overpotential and active material utilization. Some simulation-based studies have suggested this may be a promising line of enquiry [31], and building on recent developments in manufacturing capability for graded electrodes [28], we now investigate the effect of micro-scale composition grading in detail and in full cells. We design, manufacture and assess the performance of carefully controlled heterogeneous, graded electrode structures with the aim of promoting greater uniformity in overpotential distribution, and reaction rates across the electrode thickness. We investigate the arising polarization, and impedance behavior, as well as side reactions such as SEI formation. We demonstrate that micro-scale composition-graded electrodes provide enhanced capacity retention at fast charge-discharge rates and slower battery degradation in both half-cell and full-cell LIB configurations.

2. Experimental

2.1. Graded electrode fabrication

A layer-by-layer spray deposition route for supercapacitor and LIB electrodes has been developed by our group over several years (Fig. 1), and produces A5-size double-sided electrodes for pouch cells [10, 11, 32-34]. The process operates with essentially the same slurries and compositions used in the widely-used slurry casting route for the production of electrodes, but requires more dilute versions of the slurries to enable atomization into a spray that is then deposited on a current collector to form incrementally an electrode. The principal benefit is the ability to change the spray composition in time, or to mix multiple sprays, allowing electrodes with through thickness (or in-plane) variations in composition, particle size, binder fraction, discrete inter-layers, etc. to be fabricated quickly and reliably.

A planetary ball mill at 300 rpm for 1 hour (FRITSCH pulverisette 6) was used to mix electrode materials followed by high energy probe ultrasonication for 2 hours (20Hz and 750W, Vibra-cell, Sonics Inc.). The cathode active material was $LiFePO_4$ with a particle size of ~ 300 nm (Hydro-Québec, Canada), the anode active material was $Li_4Ti_5O_{12}$ spinel with a particle size of ~ 80 nm (Sigma-Aldrich), the carbon additive was Super-P (MTI, USA), the binder was PVDF (polyvinylidene fluoride, Mw~534,000, Sigma-Aldrich), and the solvent was a mixture of 1-Methyl-2-pyrrolidinone, (≥99.0%, Sigma-Aldrich) and IPA (2-propanol, 99.5%, Sigma-Aldrich) at 1 : 9 volume ratio.

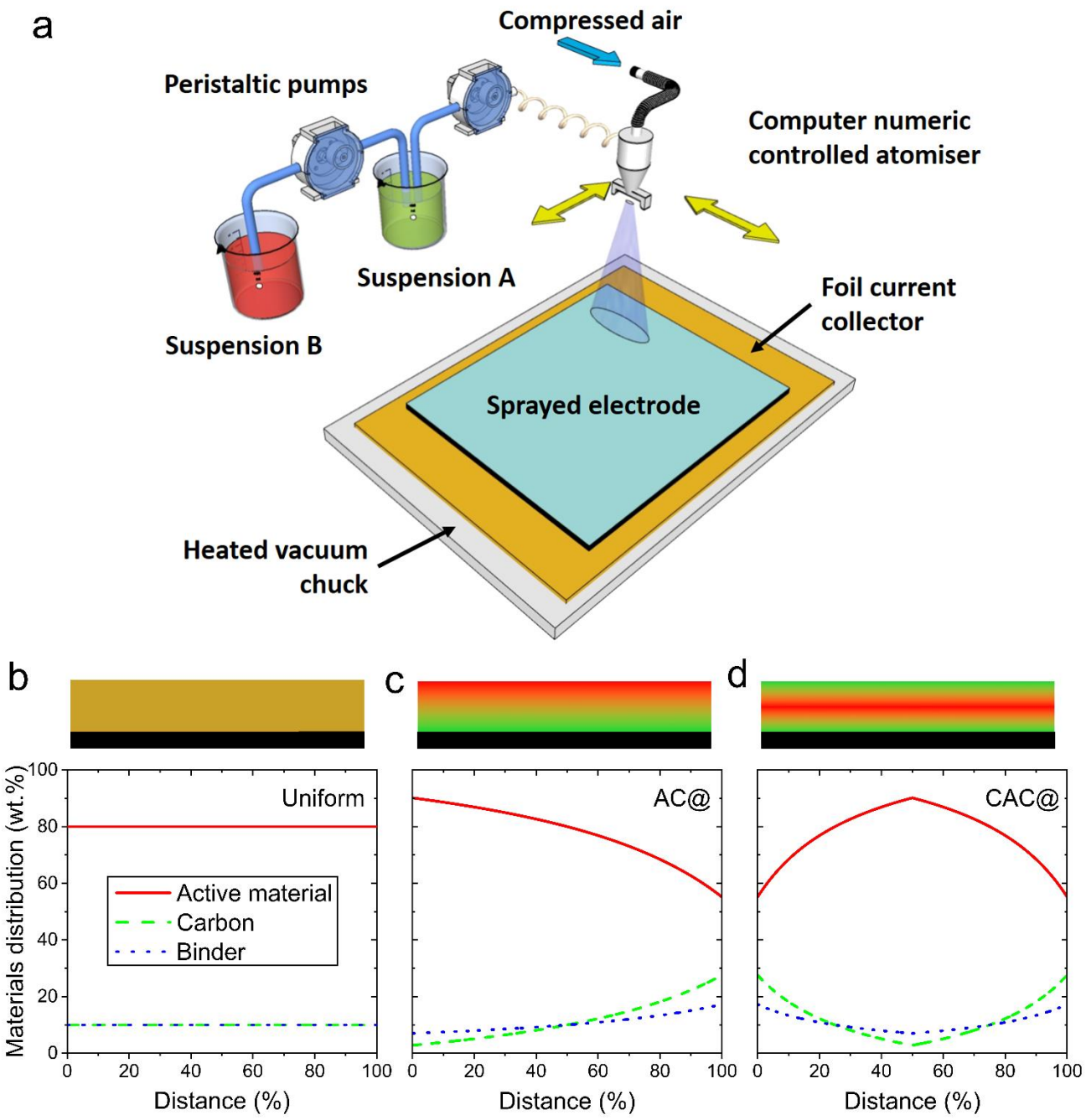

Fig. 1. (a) Illustration of the layer-by-layer spray deposition equipment for the fabrication of composition graded electrodes. (b-d) Schematic diagrams of the intended uniform, AC@ type and CAC@ type materials distribution across the thickness of the electrodes, where A (red) denotes the active material-rich region and C (green) denotes carbon black-rich region. Distance refers to the distance from the surface of the electrode (i.e. at the electrode/separator interface) towards the current collector.

Taking the fabrication of an AC@ type graded electrode as an example (Fig. 1c), suspension A with an initial weight ratio of active material:carbon:binder of 16:5:8 was pumped into an industrial spray nozzle at a controlled volumetric flow rate by a peristaltic pump, and the suspension atomized into a spray using compressed air. At the same time, suspension B with an initial weight ratio of active material:carbon:binder of 64:5:2 was pumped into suspension A to gradually change the overall weight ratios of the materials in latter suspension with time. The nozzle was attached to a stiff *x-y-z* linear manipulator gantry in which the position and speed of the nozzle was controlled by computer. The sprayed material dried almost instantaneously when deposited onto the metal foil current collector, which was attached to a heated vacuum chuck. A MATLAB® code [28] was used to calculate the required changes in composition ratio for suspensions with time in order to achieve the desired through-thickness composition gradients, which are shown schematically in Figs. 1b to 1d. For the AC@ type graded electrodes, the weight ratio of active material gradually decreased from the top surface to the current collector, while the weight ratio of carbon additive and binder gradually increased (Fig. 1c); for the CAC@ type graded electrodes, the active material was concentrated in the middle of the electrode and followed a parabola shape with thickness, while the carbon and binder was distributed in the opposite way (Fig. 1d). Overall, both AC@ and CAC@ graded electrodes had the same average weight ratio of active material: carbon: binder of 80:10:10 as the uniform electrode, and the overall weight of the sprayed electrode materials for each electrode type was kept constant, allowing a fair back-to-back comparison of electrode performance. The most critical aspect of controlling the fine-scale micro-graded structures produced by spray deposition is ensuring high suspension(s) stability over the duration of the spray fabrication step, which can vary from a few minutes to 30 min, depending on the thickness of electrode required.

2.2. Coin cell assembly

The electrodes were dried overnight at 60 ^{o}C and then calendared to 138 ± 5 µm for anodes and 109 ± 6 µm for cathodes, from which disks of 12 mm diameter were punched. The electrode material loadings were 15.8 ± 2.5 mg cm^{-2} for anodes and 15.5±1.8 mg cm^{-2} for cathodes and the overall electrode porosities were 62.1 ± 4.6% for anodes and 52.6 ± 3.8% for cathodes, based on the measurement of approximately 50 anodes and 50 cathodes. These electrode loadings were relatively high compared with some reports in the literature (3-5 mg cm^{-2}) [35, 36] but facilitated clear distinction between electrodes, both in terms of microstructural characteristics and electrochemical performance. Despite the higher electrode loadings, which may undermine capacity at

higher charge/discharge rates, the performance of some of the thick, graded electrodes was nonetheless competitive with the much lower loading and thinner electrodes more commonly found in the literature. Considering the theoretical capacity of $Li_4Ti_5O_{12}$ to be 175 mAh g^{-1} and $LiFePO_4$ to be 170 mAh g^{-1}, the areal and gravimetric capacity ratio of anode to cathode in full-cells was approximately 1.05.

Three types of CR2032 full-cells were assembled: (i) uniform cathode against uniform anode; (ii) AC@ graded cathode against AC@ graded anode, and (iii) CAC@ graded cathode against CAC@ graded anode. CR2032 half-cells were assembled with the cathode or anode working against Li foil. A Celgard separator was used and the electrolyte was 1M $LiPF_6$ in ethylene carbonate and dimethyl carbonate (EC/DMC = 50/50 v/v, Sigma-Aldrich). Care was taken to ensure that the volume of electrolyte was used in every cell. Before assembling, all cell components were stored in a vacuum oven at 70 ^oC in an Ar filled glovebox for more than 5 hours to reduce residual moisture and then assembled into cells within the same glovebox. As-assembled cells were aged for 6 to 12 hours before testing.

2.3. Electrochemical testing

Coin cells were tested using a battery cycler (Arbin Instruments, USA, Models: BT-G-25 and IBT21084LC) in the potential range 1.0 to 2.5V for full-cells, 2.5 to 4.2 V vs. Li/Li^+ for $LiFePO_4$ half-cells, and 1.0 to 2.5 V vs. Li/Li^+ for $Li_4Ti_5O_{12}$ half cells at room temperature and at various C-rates from 0.1 to 7C. Here, 0.1C corresponded to 17.0 mA g^{-1} for $LiFePO_4$ half-cells and 17.5 mA g^{-1} for $Li_4Ti_5O_{12}$ half-cells. For the full cells, the current density for C-rate tests was calculated based on the cathode capacity. Within each cycle, charging and discharging were performed at the same C-rate. Electrochemical impedance spectroscopy (EIS) was performed after discharging and aging of approximately 12 hours, with a 10 mV sine-wave perturbation in the frequency range 1 MHz down to 0.01 Hz [37-40].

2.4. Materials characterization

The cross-section of pristine electrodes was observed in a Carl-Zeiss Merlin high resolution field emission scanning electron microscope (FE-SEM) combined with an Oxford Instruments Xmax 150 energy-dispersive X-ray spectroscopy (EDX) detector. EDX mapping and line scans across the electrode thickness were performed to obtain qualitative element distributions. After battery cycling to the discharged state, anodes and cathodes from full-cells were recovered by dissembling cells in a glove box, washed in DMC (dimethyl carbonate) and then dried in glove box. X-ray Photoelectron Spectroscopy (XPS) was performed on the top-

surface of cycled electrodes (close to the separator) in a K-Alpha XPS system (Thermo Scientific). XPS samples were prepared by fixing the recovered electrodes on a sample holder in a glove box, sealed into a vacuum lock, and then transferred to the XPS system without air contamination. Quantitative analysis of XPS data was performed using CasaXPS software (Casa Software, Ltd).

3. Results and discussion

3.1. Graded materials distribution

Fig. 2 shows SEM-EDX element maps of the cross-section of fabricated $Li_4Ti_5O_{12}$-based anodes (Figs. 2a-2c) and $LiFePO_4$-based cathodes (Figs. 2d-2f), each after calendaring. The color bar below each map indicates the concentration intensity of a particular element measured by EDX. For the uniform electrodes shown in Figs. 2a and 2d, the distribution of active material (given by Ti and Fe respectively), and carbon and binder (given by C and F respectively) were approximately homogenous through the electrode thicknesses; for AC@ graded electrodes, the anode and cathode active materials showed a gradual decrease in intensity from the electrode surface to the current collector, while the carbon and binder distribution followed an opposite tendency; for CAC@ graded electrodes, the active material had the highest intensity approximately in the middle of the electrode and reduced intensity gradually towards both the electrode surface and the current collector. Overall, the experimental materials distribution conformed qualitatively to the designed distribution profiles shown in Figs. 1b-1d.

The SEM-EDX line scans across the electrodes shown in Fig. S1 further confirmed the intended, approximate uniform and graded materials distribution through electrode thickness. The traces are highlighted by the yellow lines on the SEM images in Figs. S1a-S1f. The uniform, AC@ and CAC@ electrodes showed good qualitative agreement of actual with intended composition variation shown in Figs. 1b-1d, noting that quantitative weight ratio measurement, especially for carbon, was judged insufficiently accurate by EDX.

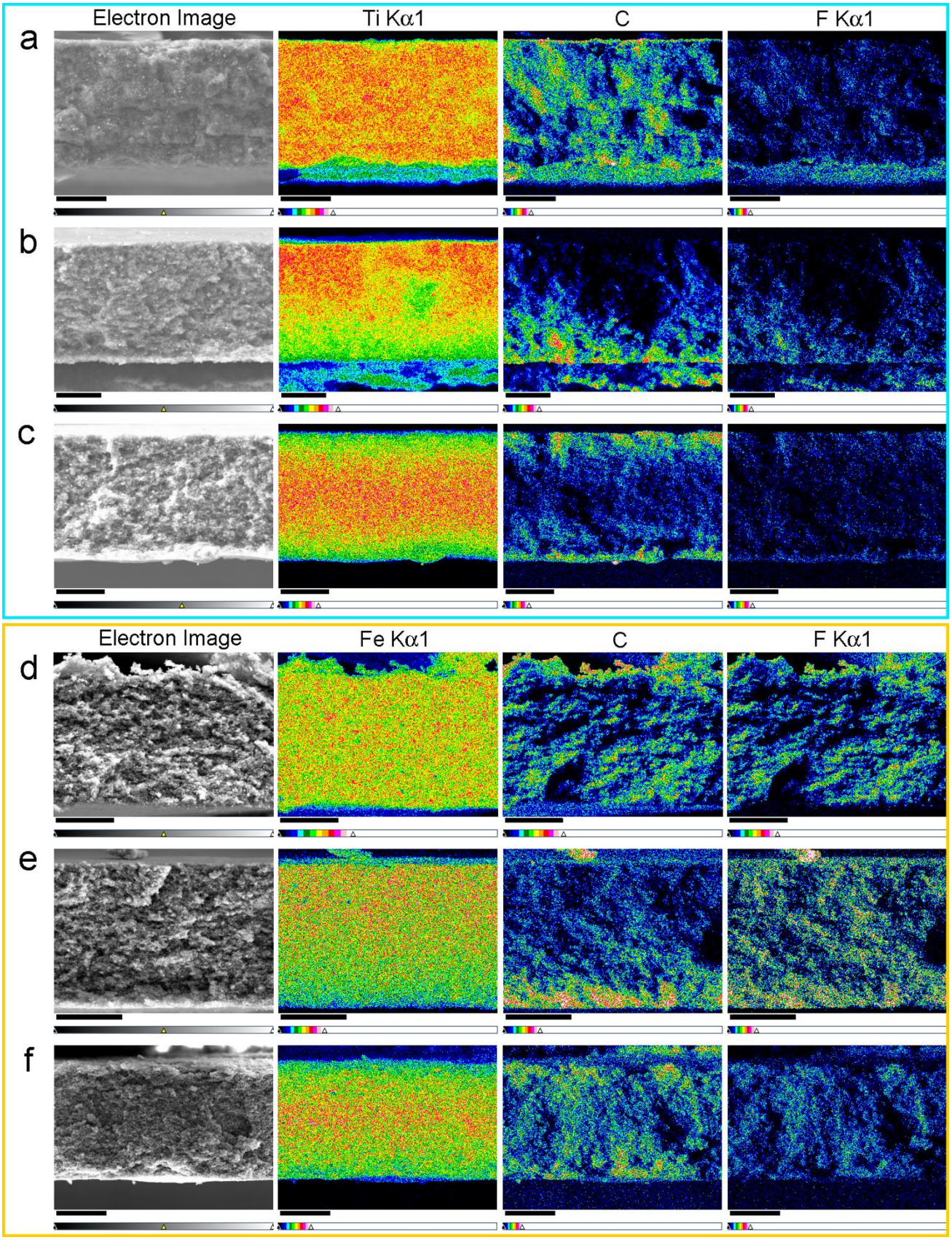

Fig. 2. SEM-EDX element maps of the cross-section of electrodes. (a-c) $Li_4Ti_5O_{12}$ based anodes and (d-f) $LiFePO_4$ based cathodes, with (a, d) uniform, (b, e) AC@ graded, and (c, f) CAC@ graded materials distribution.

The sub-figures within each figure show the SEM image, active material distribution, carbon, and binder distribution, where Ti Kα1, Fe Kα1, C, and F Kα1 are attributed to $Li_4Ti_5O_{12}$, $LiFePO_4$, carbon conductive additive and PVDF binder, respectively. Black scale bar = 50 μm.

3.2. C-rate and cycling performance

Discharge capacity from galvanostatic charge-discharge tests on half and full cells with uniform, AC@ graded and CAC@ graded electrodes at 0.1 to 7C are shown in Figs. 3a, 3c and 3e. For $Li_4Ti_5O_{12}$ half-cells at low C-rates ≤ 0.2C, both uniform and graded electrodes had similar discharge capacities, indicating that the graded material distributions did not change or sacrifice the intrinsic capacity of active materials. With C-rate increasing from 0.5 to 7C, both AC@ graded and CAC@ graded electrodes exhibited similar discharge capacities, and both higher than the uniform electrode equivalent: 3% higher at 0.5C, 16% at 2C, 41% at 3C, and 180% at 5C. These differences showed that the principal benefit of graded electrodes was to improve kinetic performance, which is further explored later.

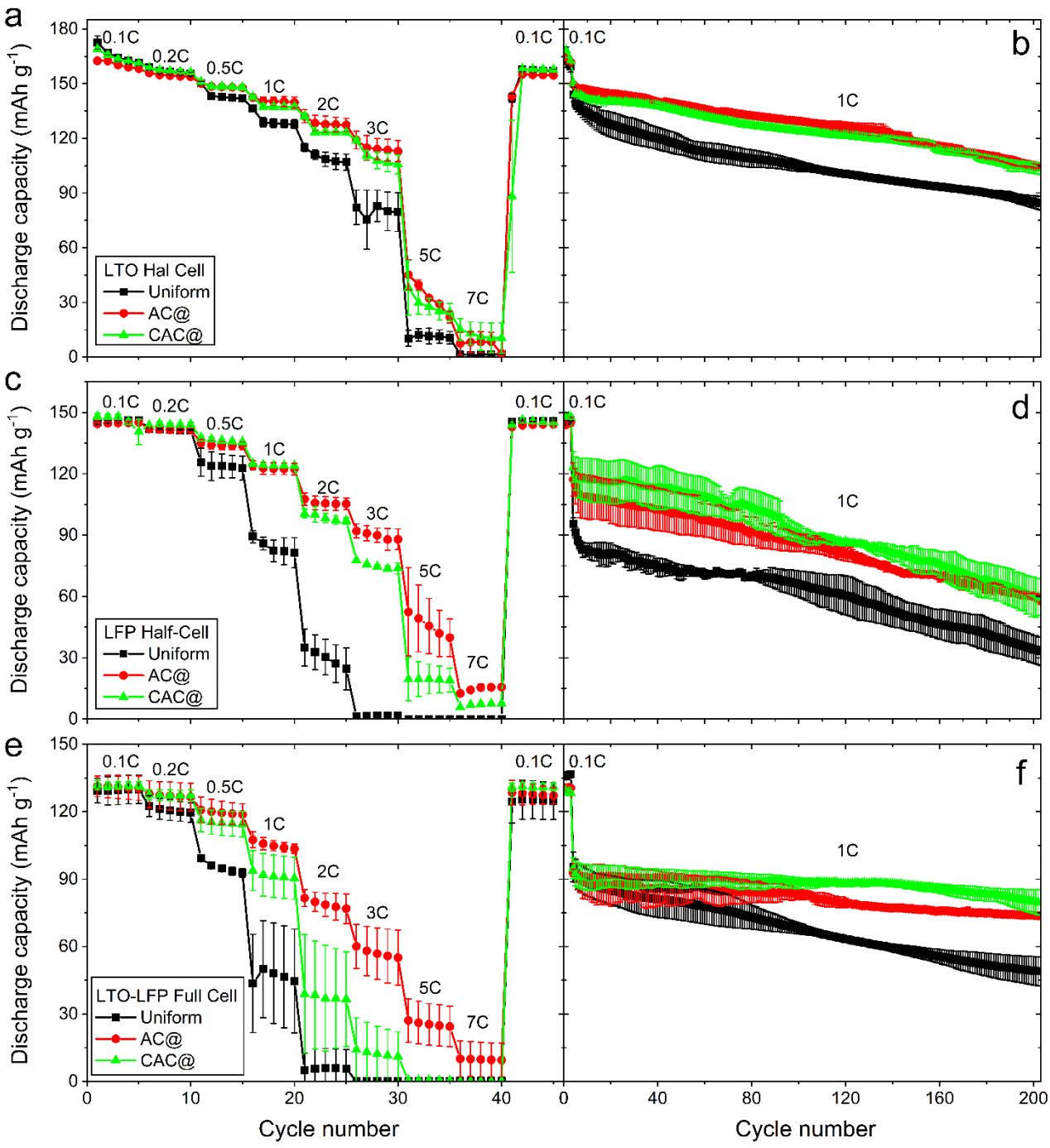

Fig. 3. (a, c, e) C-rate and (b, d, f) long-term cycling performance of (a, b) $Li_4Ti_5O_{12}$ half-cells, (c, d) $LiFePO_4$ half-cells, and (e, f) $LiFePO_4$ || $Li_4Ti_5O_{12}$ full-cells, with uniform (black), AC@ graded (red), and CAC@ graded (green) materials distributions. For long-term cycling, the first three cycles were performed at 0.1C and the following 200 cycles were performed at 1C. Two or three pristine cells were tested at each condition.

For $LiFePO_4$ half-cells in Fig. 3c, both AC@ and CAC@ graded electrodes had higher capacities than uniform electrodes from 0.5C to 7C, i.e. 9% higher at 0.5C, 240% at 2C, and 520% at 3C. The smaller relative capacity improvements by grading the $Li_4Ti_5O_{12}$ half cells compared with the graded $LiFePO_4$ half-cells was likely due to the higher porosity of $Li_4Ti_5O_{12}$-based electrodes (~62.1%) compared with the $LiFePO_4$-based electrodes (~52.6%), i.e. Li mobility was already less constrained in the $Li_4Ti_5O_{12}$ electrodes. Also, the particle size of $Li_4Ti_5O_{12}$ (~80nm) was smaller than that of $LiFePO_4$ (~300nm), which supports faster intrinsic Li insertion/deinsertion kinetics of $Li_4Ti_5O_{12}$-based electrodes; conversely electrodes based on larger-sized active particles were more effectively improved by the use of a graded structure.

Fig. 3e shows the C-rate performance of the various $LiFePO_4$ || $Li_4Ti_5O_{12}$ full-cells that were constructed with uniform cathode vs. uniform anode, AC@ graded cathode vs. AC@ graded anode, and CAC@ graded cathode vs. CAC@ graded anode. These full cells are shown schematically in Figs. 4a, 4d, and 4g, respectively. The capacity improvement due to the graded electrodes started immediately from 5% at 0.2C and then steadily increased. The difference in C-rate performance between AC@ graded and CAC@ graded electrodes became more obvious at > 1C than in half-cells (Figs. 3a and 3c) and both graded electrodes had higher capacity retention with increasing C-rate when compared with uniform electrodes: 27% at 0.5C, 120% at 1C, and 1300% at 2C for AC@ graded electrodes; and 21% at 0.5C, 97% at 1C, 570% at 2C for CAC@ graded electrodes.

Overall, the superior performance of graded electrodes previously shown for half-cells was enhanced in the full-cells. For example, compared with uniform electrodes at 1C, both AC@ and CAC@ graded electrodes increased capacity by 7% in $Li_4Ti_5O_{12}$ half-cells and by 47% in $LiFePO_4$ half-cells; while for $LiFePO_4$ ||$Li_4Ti_5O_{12}$ full-cells, the AC@ and CAC@ graded electrodes increased capacity by 126% and 97%, respectively.

During long-term cycling shown in Figs. 3b, 3d, and 3f, graded electrodes retained capacity better than uniform electrodes. After 200 cycles at 1C, discharge capacities for uniform, AC@ graded and CAC@ graded electrodes were 84 mAh g^{-1}, 104 mAh g^{-1} and 103 mAh g^{-1} in $Li_4Ti_5O_{12}$ half-cells; 33 mAh g^{-1}, 58 mAh g^{-1}, and 60 mAh g^{-1} in $LiFePO_4$ half-cells; and 49 mAh g^{-1}, 74 mAh g^{-1} and 80 mAh g^{-1} for $LiFePO_4$ || $Li_4Ti_5O_{12}$ full-cells. The capacity degradation rate for $Li_4Ti_5O_{12}$ half-cells and $LiFePO_4$ half-cells were ~0.2 and ~0.3 mAh g^{-1} per cycle, respectively, with no obvious difference between uniform and graded electrodes; however, in the full-cells, the capacity degradation rates for the uniform, AC@ graded and CAC@ graded electrodes were 0.21,

0.08, and 0.05 mAh g^{-1} per cycle, respectively, i.e. the degradation rate of graded electrode full cells was less than half that of cells with uniform electrodes.

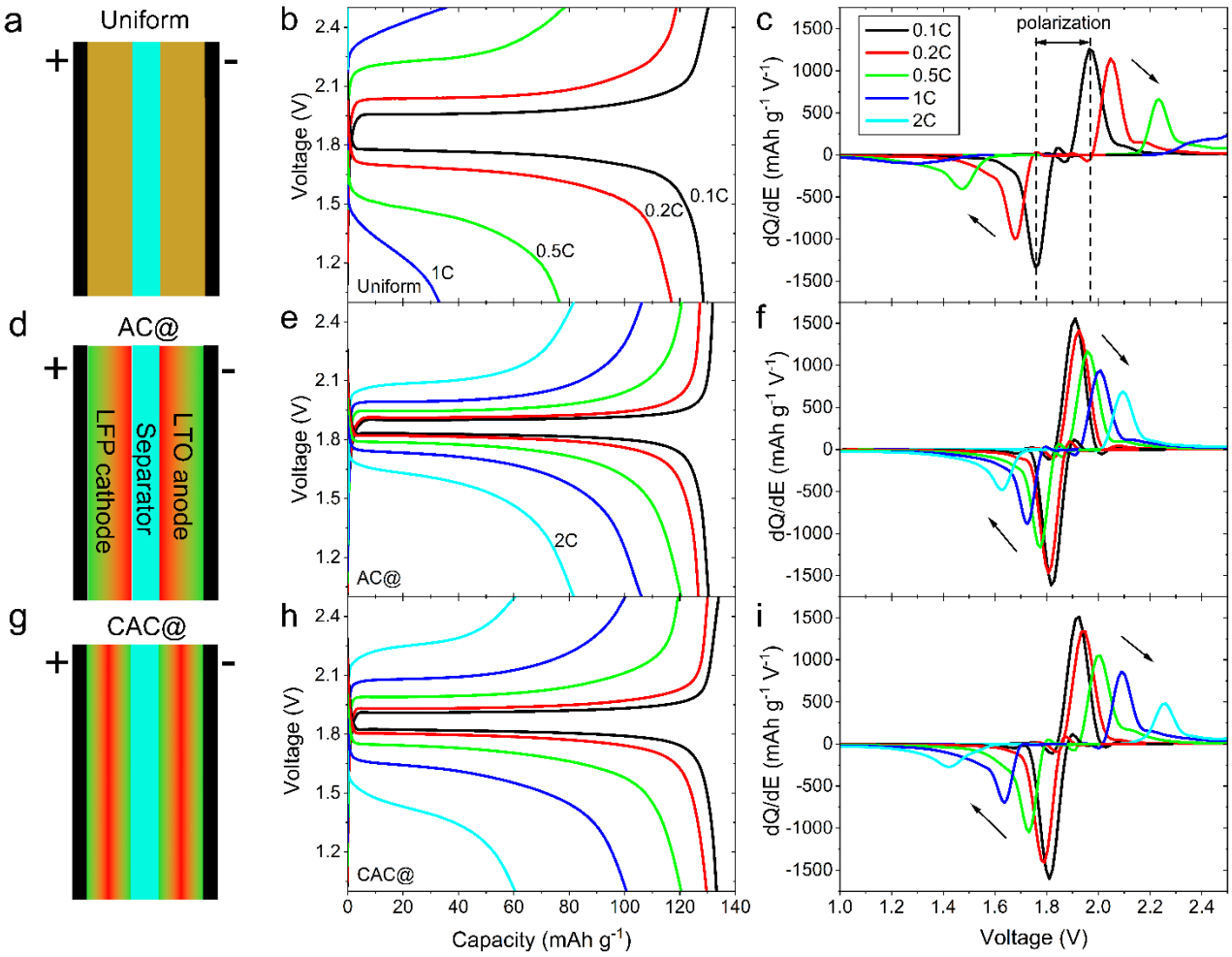

Fig. 4. (a, d, g) Schematic illustration of the $LiFePO_4$ || $Li_4Ti_5O_{12}$ full-cell configurations with uniform, AC@ graded and CAC@ graded materials distribution, respectively. (b, e, h) Galvanostatic charge-discharge curves of the full-cells at 0.1, 0.2, 0.5, 1 and 2C, respectively. (c, f, i) first derivatives of capacity with respect to voltage (dQ/dE) against voltage corresponding to (b, e, h), respectively.

3.3. Cell polarization

Figs. 4b, 4e, and 4h show the full-cell charge and discharge profiles. As previously described, the uniform electrode cell capacity decreased faster than the AC@ and CAC@ graded full-cells, although they had similar capacities at 0.1C. To investigate cell polarization effects, defined as the potential difference between charge and discharge curves, the 1st derivative of the charge-discharge profiles (dQ/dE) was plotted as a function

of voltage in Figs. 4c, 4f and 4i, where *Q* is the capacitance and *E* is voltage. The polarization was assessed by comparing the potential difference in first derivative peaks in charge and discharge plots at the same C-rate, with an example indicated by the dashed line in Fig. 4c. Figs. 4c, 4f and 4i show the polarization of uniform full-cells increased faster than graded cells with increasing C-rate. The polarizations were measured only up to 3C because beyond 3C, the uniform electrode cell did not provide obvious peaks due to severe capacity decay.

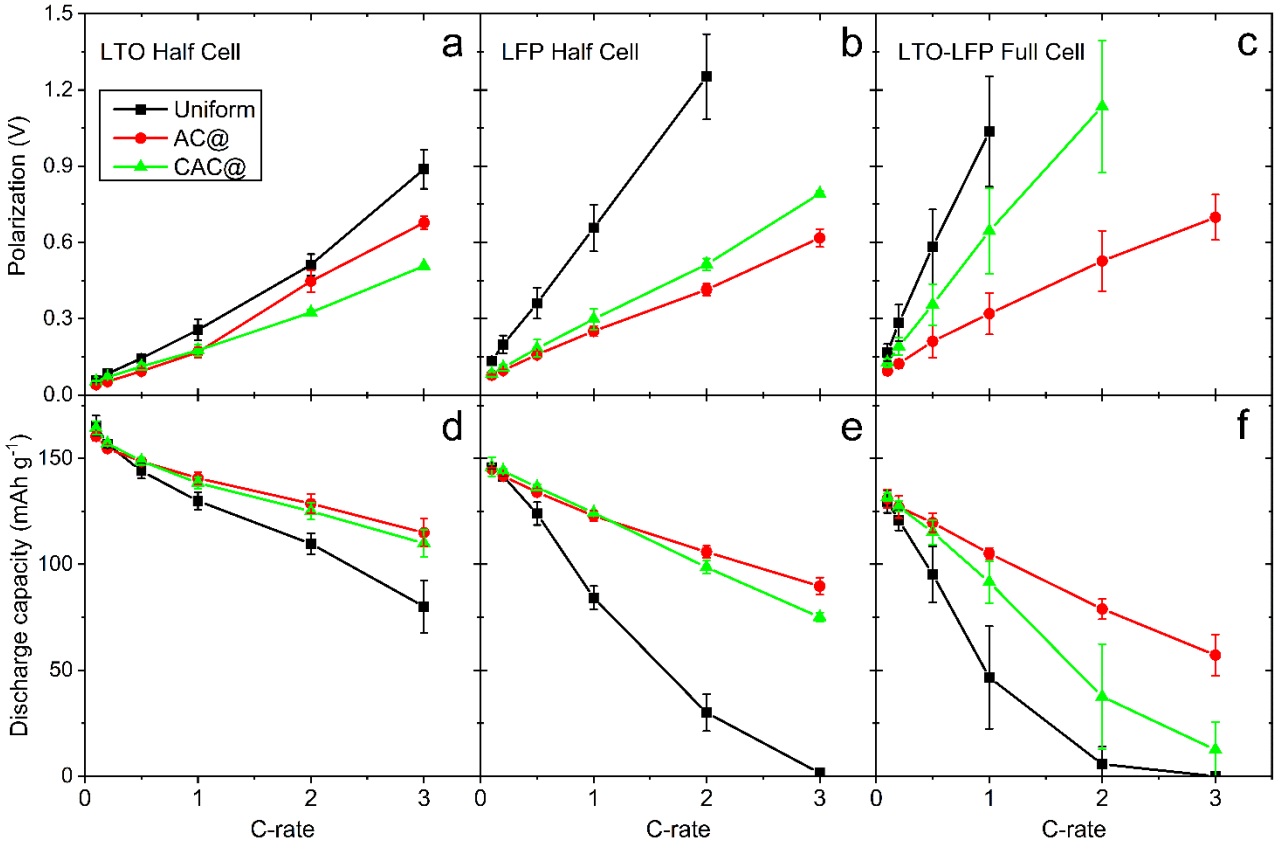

Fig. 5. (a, b, c) Polarization obtained from the voltage difference between galvanostatic charge and discharge curves as a function of C-rate, and (d-f) Discharge capacity as a function of C-rates, for $Li_4Ti_5O_{12}$ half-cell, $LiFePO_4$ half-cell, and $LiFePO_4$ || $Li_4Ti_5O_{12}$ full-cell, respectively.

Figs. 5a to 5c show these trends in more detail by plotting the cell polarization of $Li_4Ti_5O_{12}$ half-cells, $LiFePO_4$ half-cells, and $LiFePO_4$ || $Li_4Ti_5O_{12}$ full cells as a function of C-rate. For both half and full cells, the cell polarization increased almost linearly with C-rate, however, the polarization of uniform electrode cells increased much faster than graded electrode cells. Figs. 5d to 5f show the discharge capacities of the same cells, again as a function of C-rate. The larger polarization difference generally corresponded to a more rapid loss of

capacity. Consolidating these data, Fig. S2 shows that discharge capacity had an approximate linear decrease with increasing polarization, regardless of whether uniform or graded electrodes. The overlapping data between $Li_4Ti_5O_{12}$ and $LiFePO_4$ half-cells in Fig. S2 was due to their similar theoretical capacities. Because the cell polarization usually reflects the cell resistance, the charge transfer resistance of the same graded and uniform cell arrangements was investigated further by electrochemical impedance spectroscopy (EIS).

3.4. Electrochemical impedance spectroscopy

After C-rate testing in Figs. 3a, 3c, 3e, and long-term cycling in Fig. 3f, cells were investigated by EIS in the discharged states for $LiFePO_4$ half-cells and $LiFePO_4$ || $Li_4Ti_5O_{12}$ full cells, and at the charged state for $Li_4Ti_5O_{12}$ half-cells, as shown in Figs. 6a to 6d. The charge transfer resistance (R_{ct}) can be obtained by numerical fitting of EIS data to an equivalent circuit shown in Fig. 6e, and R_{ct} is plotted in Fig. 6f (left). All other fitting parameters are provided in Table S1 in the Supplementary Data. The best-fit to the EIS data is shown as solid lines in Figs. 6a to 6d, indicating a reasonable fit for all cells. The time constant $\tau = R_{ct}C_{eff}$, where C_{eff} is the effective capacity of the constant phase element CPE2 in the equivalent circuit that expresses the time required for charge transfer during redox reactions, was below 1 ms for each cell (Fig. 6f, right). For both half and full cells, the AC@ and CAC@ graded electrodes had smaller charge transfer resistance than for uniform cells. Differences in time constant followed the same trend as charge transfer resistance (Fig. 6f, right).

The difference in charge transfer resistance between different types of $Li_4Ti_5O_{12}$ half-cells was smaller than those between different types of $LiFePO_4$ half-cells, again likely due to the higher porosity of the $Li_4Ti_5O_{12}$-based anodes and their smaller active particle size. Moreover, the greatest difference in charge transfer resistance between graded and uniform cells was for full-cells, whose charge transfer resistance was mainly due to the cathode rather than the anode (Fig. 6f, left). After long-term cycling of full cells (1C for 200 cycles), Fig. 6d also shows that the smaller charge transfer resistance of graded electrodes was maintained. Although the full cells cycled in Figs. 6c and 6d experienced a different testing history, the AC@ graded electrodes had an obvious increase in charge transfer resistance after long-term cycling (Fig. 6f, left), while CAC@ graded electrodes were relatively stable. Overall, the CAC@ type electrodes had the best long-term cycling performance.

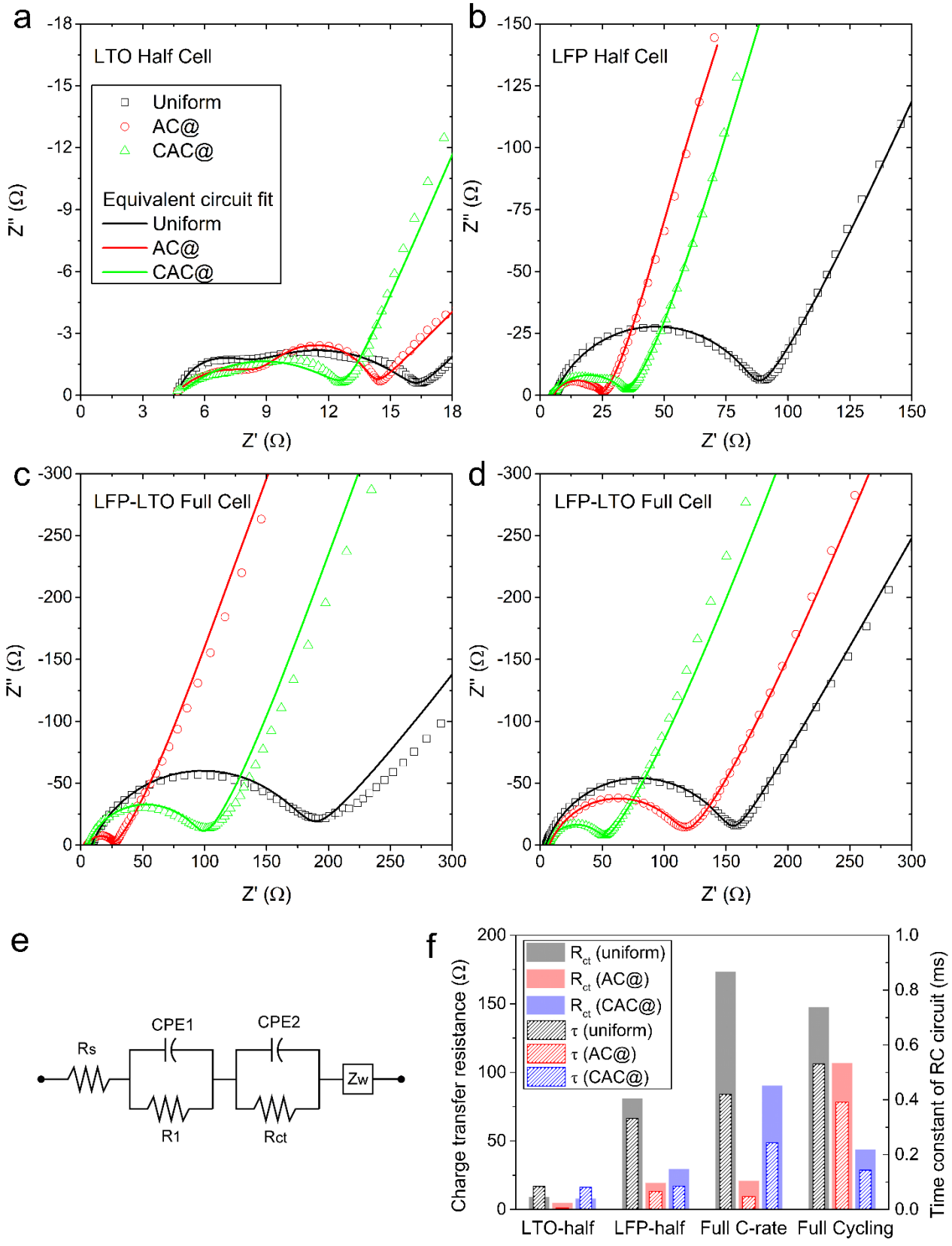

Fig. 6. (a-c) Electrochemical impedance spectroscopy (EIS) Nyquist plots for $Li_4Ti_5O_{12}$ (LTO) half-cells, $LiFePO_4$ (LFP) half-cells, LTO-LFP full-cells after C-rate testing shown in Figs. 3a, 3c and 3e, respectively. (d)

Nyquist plot for LTO-LFP full-cells after 200 cycles at 1C shown in Fig. 3f. (e) Equivalent circuit for EIS fitting. The best-fit data is shown by the solid lines in (a-d). (f) Charge transfer resistance (R_{ct}, left) and time constant ($\tau = R_{ct}C_{eff}$, right) for charge transfer, where C_{eff} is the effective capacity of the constant phase element, CPE2, in the equivalent circuit shown in (e). Along the *x*-axis, LTO-half, LFP-half, Full C-rate, and Full Cycling correspond to the cells in (a), (b), (c), and (d), respectively.

The data in Fig. 6f shows that the resistance of graded electrodes was reduced compared with uniform equivalents, and time constants were also reduced (consistent with the polarization data shown earlier). In order to understand this behaviour step further, five sprayed, uniform $LiFePO_4$-based electrodes with different $LiFePO_4$: carbon : binder ratios to represent the range of ratios created across a graded electrode (Fig. S4a) were manufactured. Further details are given in the Supplementary Data. After the usual amount of calendaring, the electrical conductivity of each electrode was measured in a special jig (Fig. S4b), along with the average electrode porosity as described in the Supplementary Data. In this way the local electrical conductivity and porosity was determined as a function of local composition within a graded electrode, which can be thought of as comprising sub-layers of uniform electrodes with different composition stacked on top of one another (Fig. S4c). These data showed that increasing the local conductive carbon fraction increased not only the local electrical conductivity i.e. reduced the local resistance, but also increased the local porosity. It is these effects combined, especially when the carbon-rich part of the graded electrode is placed against the current collector, which underpins the superior electrochemical response of the graded electrodes.

It can be conjectured that it would be useful to decouple and probe the relative contributions of local conductivity and local porosity on overall electrode performance even further. However in practice, there is not yet a manufacturing process that can produce realistic electrodes with control of *local* conductivity and porosity *independently* while keeping average composition and material loadings constant. A more fruitful approach may be to undertake parametric studies using an appropriate numerical model, calibrated with data of the type presented here, to probe their relative contributions to performance enhancement.

3.5. XPS analysis of cycled electrodes

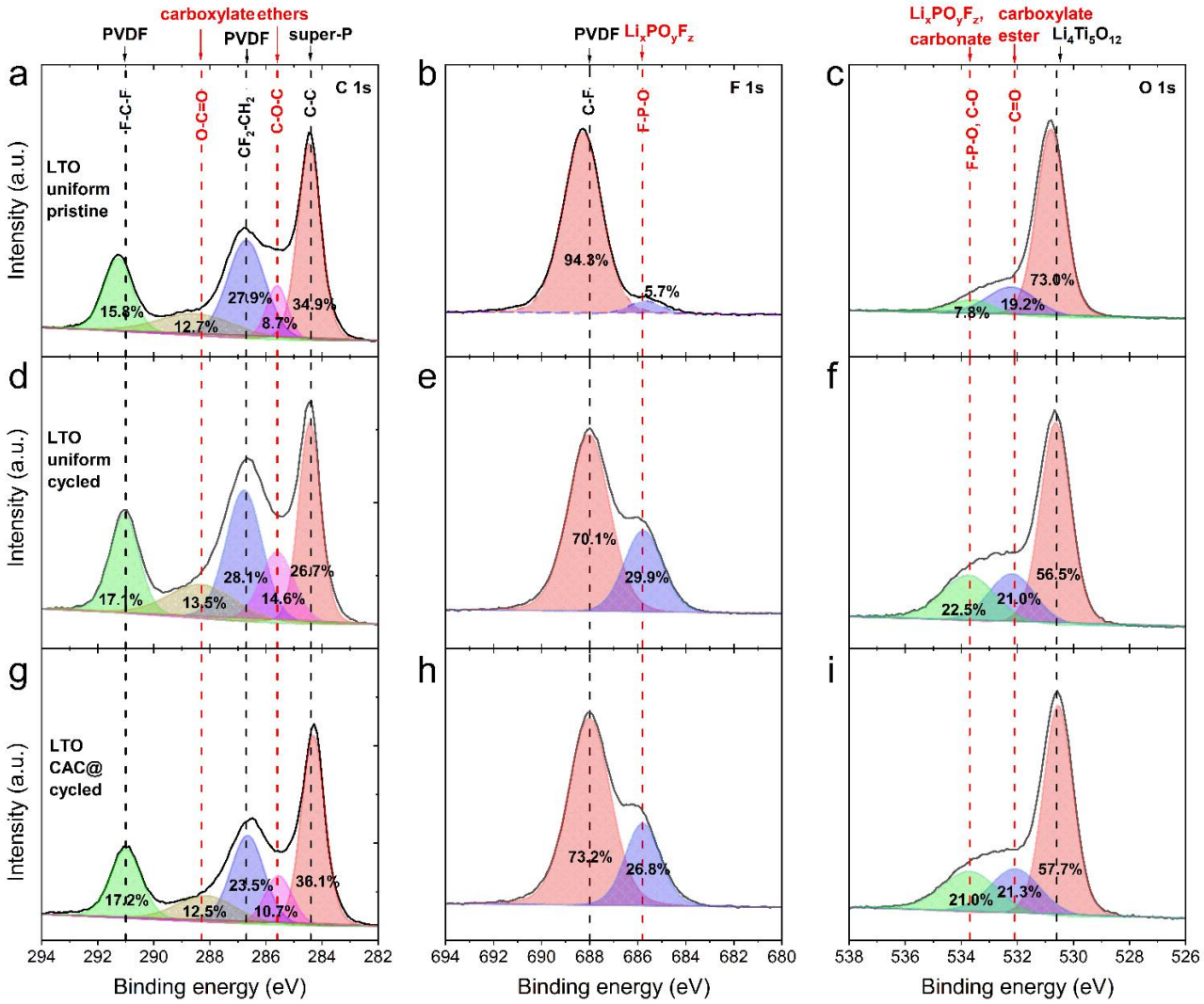

Fig. 7. X-ray photoelectron spectra (XPS) of $Li_4Ti_5O_{12}$-based anodes recovered from full-cells after 200 cycles at 1C in Fig. 3f. (a-c) pristine (no-cycles) uniform anode, (d-f) cycled uniform anode, and (g-i) cycled CAC@ graded anode. (a, d, g) C 1s spectra, (b, e, h) F 1s spectra, and (c, f, i) O 1s spectra. The vertical dashed lines indicate the labelled reference chemical bonds taken from the literature [26, 27, 41-43]. The estimated atomic ratios of C, F and O obtained by peak deconvolution and integration (filled regions) are noted on the plots.

The full-cell batteries cycled in Fig. 3f were investigated by X-ray photoelectron spectra (XPS) characterization and Fig. 7 shows XPS spectra for a $Li_4Ti_5O_{12}$-based anode after cycling. From the C 1s spectra shown in Figs. 7a, 7d and 7g, both uniform and graded electrodes had a higher fraction of C-O single bond and C=O double bonds at 285.6 eV and 288.3 eV after cycling [44], which was attributed to ethers and carboxylates, respectively. By using peak deconvolution the C-C bond due to the Super-P conductivity enhancer additive as

a reference, the atomic ratio of C-O : C-C was 0.55 and 0.30 for cycled uniform and CAC@ graded anodes, respectively; the ratio of C=O : C-C was 0.51 and 0.35 for cycled uniform and CAC@ graded anodes, respectively. By assuming that ethers and carboxylates can be attributed to the solid electrolyte interphase (SEI) [41-43], these data support less SEI formation in the graded electrode. Although limited SEI formation on the active material of the anode is helpful to stabilize the electrode/electrolyte interface, too much SEI will increase the impedance of the electrode, and thus, can be expected to increase polarization and reduce C-rate performance.

The F1s spectra in Figs. 7b, 7e, and 7h show that the contribution of the F-P bond (685.8 eV) associated with $Li_xPO_yF_z$ increased strongly after cycling due to the decomposition of the $LiPF_6$ salt in the electrolyte [41]. Again using peak deconvolution, the atomic ratio of F associated with the P-F bond to that associated with PVDF binder (P-F : C-F) was estimated as 0.43 and 0.37 for cycled uniform and CAC@ anodes, respectively, which again may be interpreted as less SEI formation in the CAC@ graded anode. From the O 1s spectra shown in Figs. 7c, 7f, and 7i, both cycled uniform and CAC@ graded anodes developed more intense C-O (or P-O) single bond (533.7eV) and C=O double bonds (532.1eV) after cycling, again due to electrolyte degradation at the surface of electrode. Using the deconvoluted O peak within $Li_4Ti_5O_{12}$ as a reference, the ratios of (C-O plus C=O) : $Li_4Ti_5O_{12}$ were 0.78 and 0.73 for cycled uniform and CAC@ graded anodes. Therefore, from C1s, F1s, and O1s spectra, it can be reasonably hypothesized that SEI formed in the CAC@ graded electrode was either thinner and / or at lower overall fraction, and helps to explain its better C-rate performance, lower polarization, and smaller charge transfer resistance when compared with a uniform electrode (Figs. 5 and 6).

Following a similar approach, Fig. S3 shows the XPS spectra for the $LiFePO_4$-based cathodes recovered from full-cells after 200 cycles at 1C. From the C 1s spectra in Figs. S3a, S3d and S3g, the cycled AC@ graded and CAC@ graded cathodes have less C-O single bond and C=O double bond content compared with the same cycled uniform cathodes. For example, the atomic ratio of C associated with C-O to C-C was 0.77, 0.41 and 0.27 for the cycled uniform, AC@ and CAC@ cathodes respectively, which supported less/thinner SEI formation on the graded cathodes. From F 1s spectra shown in Figs. S3b, S3e and S3h, the F-P-O bond attributed to the SEI component of $Li_xPO_yF_z$ contributed less of the overall spectrum for the cycled graded electrodes. With the F response in the PVDF binder as a reference, the atomic ratio of F associated with F-P-O ($Li_xPO_yF_z$) to C-F (PVDF) was 0.45, 0.34 and 0.23 for uniform, AC@ graded and CAC@ graded cathodes, respectively. From the P 2p spectra, the atomic ratio of P associated with F-P-O ($Li_xPO_yF_z$) to $LiFePO_4$ is 1.20, 0.43 and 0.35

for uniform, AC@ graded and CAC@ graded cathodes, respectively. Therefore, XPS data from cycled cathodes also strongly suggested that SEI formation on AC@ and CAC@ graded electrodes was reduced. Across anodes and cathodes, a consistent picture emerged of reduced SEI formation in graded electrodes that supported their more favorable energy storage response over otherwise identical uniform electrodes. To reinforce these findings, various avenues to obtain spatially resolved XPS spectra across a single electrode, either by (i) depth profiling "down" through an electrode or (ii) from discrete locations across an electrode cross-section were explored. At the time of writing no such data of sufficient spatial resolution to be helpful could be obtained, but remains an active line of enquiry.

Using simulation, grading of the type explored here has been suggested to modify and homogenize the spatial distribution of the electrode overpotential [31]. The experimental work here provides cell data consistent with this prior suggestion and for the first time quantifies the marked benefits of grading by experiment. The manufacturing technology is now available to produce electrodes with practically any arbitrary spatial arrangement of materials, and it seems likely that even more potent gradations might exist, and may allow significant cell improvements without the need for new electrochemical systems. On the other hand, new even higher performing electrochemical systems may be enabled, for example, electrodes composed of local mixtures of materials contrived to best exploit the particular local overpotential and other conditions at that specific point in the electrode, and this forms part of our ongoing work.

Given the importance of grading on local electrical conductivity and its strong influence on overall electrode performance shown here, future work might also consider how conducting carbon grading effects change, or might be used to manage, internal ohmic heating effects, particularly once electrodes are stacked or wound into planar or cylindrical multi-layers.

3.6. Ragone plots

Figs. 8a-c summarize the gravimetric power density against energy density (Ragone plots) for $LiFePO_4$ || $Li_4Ti_5O_{12}$ full-cells, $LiFePO_4$-based half-cells and $Li_4Ti_5O_{12}$-based half-cells, respectively. Both full and half cells share some common features: cells with uniform, AC@ graded, and CAC@ graded electrodes have the same maximum energy densities and minimum power densities, which was determined by the intrinsic energy storage capability of the active materials. The $Li_4Ti_5O_{12}$-based half-cells in Fig. 8c showed a relatively narrow band of energy-power combinations over the range studied, consistent with previous results and the higher

porosity/smaller particle size in these electrodes. In contrast, the $LiFePO_4$-based half-cells in Fig. 8b showed strong sensitivity to structure at intermediate energy-power densities, with graded electrodes significantly outperforming uniform equivalents. In full cells, the benefit of grading – particularly in the cathode – were carried over, so that, for example, at an intermediate power density of 120 W kg^{-1}, the graded cells provided a ~65% increase in energy density over uniform cells. To demonstrate scalability, Fig. 8d show an as-sprayed $LiFePO_4$-based electrode with area ~23 × 23 cm^2 that was manufactured using a single spray nozzle. Adding more nozzles to increase production rate is straightforward.

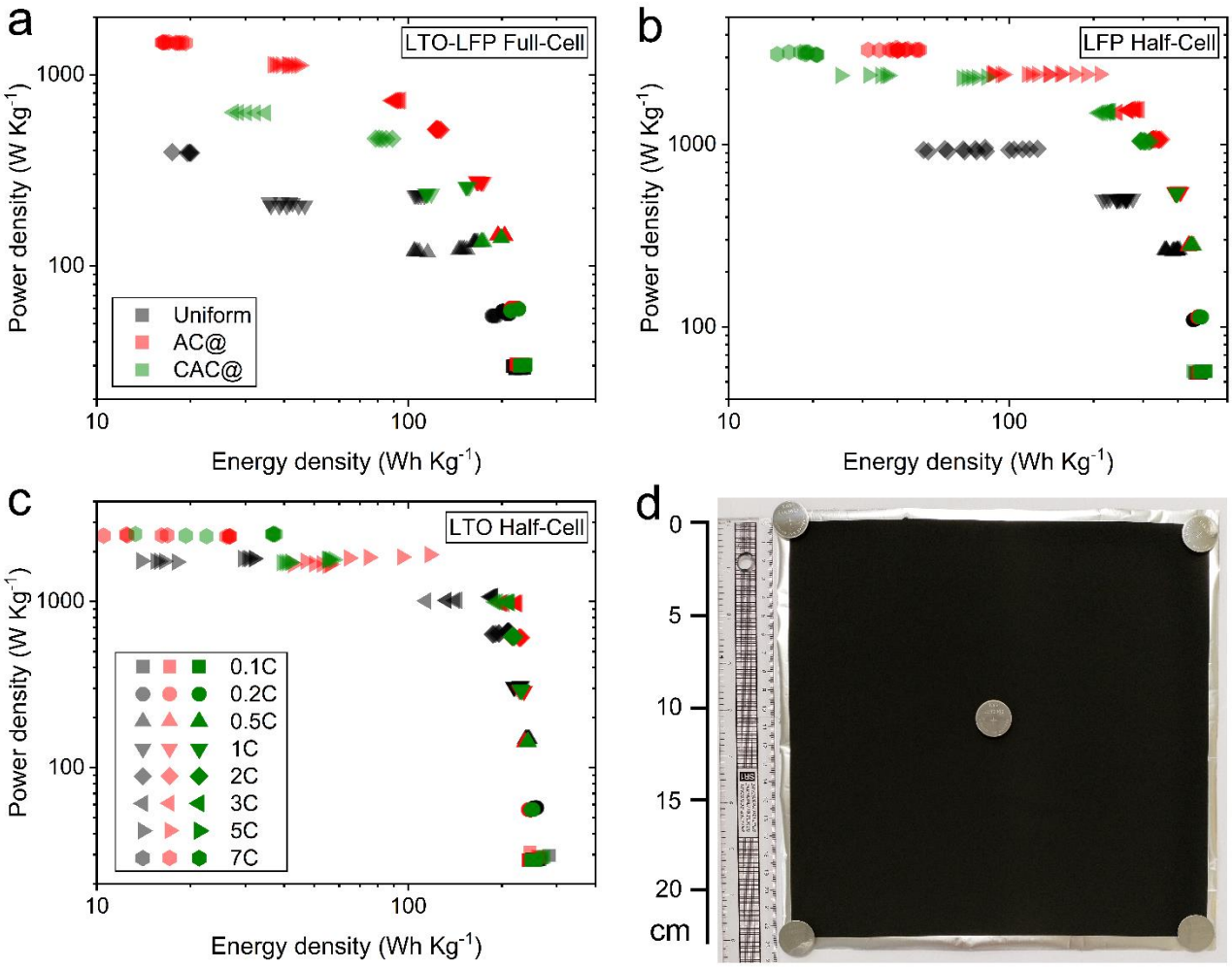

Fig. 8. (a-c) Ragone plots of $LiFePO_4$ || $Li_4Ti_5O_{12}$ full-cells, $LiFePO_4$-based half-cells and $Li_4Ti_5O_{12}$-based half-cells, respectively. (d) Example photo of an as-sprayed $LiFePO_4$-based cathode (area ~23 × 23 cm^2) on Al foil current collector. Five assembled CR2032 coin cells were used to show the scale difference.

The suspension deposition route described here allows almost any arbitrary arrangement of active, binder and conducting material through the electrode thickness to be realized, representing myriad possibilities for performance optimization. Unfortunately, intuition or simple theory can be a poor guide to quickly realizing the optimum materials arrangement because so many parameters interact with one another in complex ways, and there are too many possibilities for trial and error. Thus there is an opportunity for numerical models to play a facilitating role in guiding electrode structural optimization for graded, layered or other hetero-electrodes [45, 46], providing that these models can represent the micro-scale control we can now achieve experimentally. Guided by effective optimization routines, novel balances of capacity, power and lifetime might be achieved, across a wide range of cell chemistries.

4. Conclusions

We have demonstrated that designed electrode hetero-structures for use in Li-ion batteries can be an effective way to improve the C-rate and long-term cycling performance compared with uniform but otherwise identical electrodes. $Li_4Ti_5O_{12}$ based anodes and $LiFePO_4$ based cathodes were fabricated by layer-by-layer spray printing that readily facilitated a gradient materials distribution through the electrode thickness with micro-scale resolution, and allowed a fair back-to-back comparison with uniform structure electrodes. An improvement in C-rate performance of up to 126% at 1C was achieved in full-cells with gradient material distributions in both the anode and cathode when compared with full-cells with uniform and otherwise identical electrodes. Full-cells with graded electrodes amplified improvements seen in the $Li_4Ti_5O_{12}$ and the $LiFePO_4$ half-cells. The benefits of graded electrodes were more marked for larger diameter active particles, closer to the type preferably used in commercial cells. During long-term cycling, the capacity degradation of full-cells with graded electrodes was less than half of full-cells with uniform electrodes.

The improved capacity and power performance of graded cells was due to lower cell polarizations compared with uniform electrodes, which was most marked with increasing C-rate. Accordingly, the charge transfer resistance of full-cells with graded electrodes was lower than for uniform electrodes. XPS surface analysis of cycled electrodes showed less SEI formation on graded electrodes, which was consistent with measured lower charge transfer resistances. The origin of the advantage of graded electrodes is suggested to arise from the homogenization of local overpotential distribution through the electrode thickness.

Acknowledgments

This work was supported by the UK Engineering and Physical Sciences Research Council (EPSRC) through grant EP/P005411/1 “Structured electrodes for improved energy storage” with some capital equipment provided by the Henry Royce Institute through EPSRC grant EP/R010145/1. We would like to thank Philip Holdway for XPS characterization, and Hydro-Québec (Canada) for providing the $LiFePO_4$.

Appendix A. Supplementary data

Supplementary data related to this article can be found at https://doi.org/###

References

[1] J.L. Li, C. Daniel, D.L. Wood, Cathode manufacturing for lithium-ion batteries, in: C. Daniel, J.O. Besenhard (Eds.) Handbook of Battery Materials, Wiley-VCH, 2011, pp. 939-960.

[2] J.L. Li, Z.J. Du, R.E. Ruther, S.J. An, L.A. David, K. Hays, M. Wood, N.D. Phillip, Y.P. Sheng, C.Y. Mao, S. Kalnaus, C. Daniel, D.L. Wood, Toward low-cost, high-energy density, and high-power density lithium-ion batteries, JOM, 69 (2017) 1484-1496.

[3] R. Zhao, J. Liu, J. Gu, The effects of electrode thickness on the electrochemical and thermal characteristics of lithium ion battery, Appl. Energy, 139 (2015) 220-229.

[4] J.S. Sander, R.M. Erb, L. Li, A. Gurijala, Y.M. Chiang, High-performance battery electrodes via magnetic templating, Nat. Energy, 1 (2016) 16099-1-6.

[5] J. Billaud, F. Bouville, T. Magrini, C. Villevieille, A.R. Studart, Magnetically aligned graphite electrodes for high-rate performance Li-ion batteries, Nat. Energy, 1 (2016) 16097-1-6.

[6] C.J. Bae, C.K. Erdonmez, J.W. Halloran, Y.M. Chiang, Design of battery electrodes with dual-scale porosity to minimize tortuosity and maximize performance, Adv. Mater., 25 (2013) 1254-1258.

[7] S. Behr, R. Amin, Y.M. Chiang, A.P. Tomsia, Highly-structured, additive-free lithium-ion cathodes by freeze-casting technology, Process Eng., 92 (2015) E39-E43.

[8] L. Li, R.M. Erb, J. Wang, J. Wang, Y.-M. Chiang, Fabrication of low-tortuosity ultrahigh-area-capacity battery electrodes through magnetic alignment of emulsion-based slurries, Adv. Energy Mater, 9 (2019) 1802472-1-7.

[9] L. Liu, P.J. Guan, C.H. Liu, Experimental and simulation investigations of porosity graded cathodes in mitigating battery degradation of high voltage lithium-ion batteries, J. Electrochem. Soc., 164 (2017) A3163-A3173.

[10] C. Huang, N.P. Young, J. Zhang, H.J. Snaith, P.S. Grant, A two layer electrode structure for improved Li Ion diffusion and volumetric capacity in Li Ion batteries, Nano Energy, 31 (2017) 377-385.

[11] C. Huang, A. Kim, D.J. Chung, E. Park, N.P. Young, K. Jurkschat, H. Kim, P.S. Grant, Multi-scale engineered Si-SiO_2 nanocomposite electrodes for lithium ion batteries using layer-by-layer spray deposition, ACS Appl. Mater. Interfaces, 10 (2018) 15624-15633.

[12] N. Meethong, Y.H. Kao, W.C. Carter, Y.M. Chiang, Comparative study of lithium transport kinetics in olivine cathodes for Li-ion batteries, Chem. Mater., 22 (2010) 1088-1097.

[13] L. David, R.E. Ruther, D. Mohanty, H.M. Meyer, Y. Sheng, S. Kalnaus, C. Daniel, D.L. Wood, Identifying degradation mechanisms in lithium-ion batteries with coating defects at the cathode, Appl. Energy, 231 (2018) 446-455.

[14] E. Hosseinzadeh, J. Marco, P. Jennings, The impact of multi-layered porosity distribution on the performance of a lithium ion battery, Appl. Math. Modell., 61 (2018) 107-123.

[15] E. Hosseinzadeh, R. Genieser, D. Worwood, A. Barai, J. Marco, P. Jennings, A systematic approach for electrochemical-thermal modelling of a large format lithium-ion battery for electric vehicle application, J. Power Sources, 382 (2018) 77-94.

[16] J. Lu, Z.H. Chen, Z.F. Ma, F. Pan, L.A. Curtiss, K. Amine, The role of nanotechnology in the development of battery materials for electric vehicles, Nat. Nanotechnol., 11 (2016) 1031-1038.

[17] J. Jaguemont, L. Boulon, Y. Dubé, A comprehensive review of lithium-ion batteries used in hybrid and electric vehicles at cold temperatures, Appl. Energy, 164 (2016) 99-114.

[18] F.H. Gandoman, J. Jaguemont, S. Goutam, R. Gopalakrishnan, Y. Firouz, T. Kalogiannis, N. Omar, J. Van Mierlo, Concept of reliability and safety assessment of lithium-ion batteries in electric vehicles: Basics, progress, and challenges, Appl. Energy, 251 (2019) 113343-1-17.

[19] Z.Y. Jiang, Z.G. Qu, L. Zhou, W.Q. Tao, A microscopic investigation of ion and electron transport in lithium-ion battery porous electrodes using the lattice Boltzmann method, Appl. Energy, 194 (2017) 530-539.
[20] T.R. Ashwin, A. McGordon, P.A. Jennings, A mass transfer based variable porosity model with particle radius change for a Lithium-ion battery, Electrochim. Acta, 232 (2017) 203-214.
[21] V.P. Nemani, S.J. Harris, K.C. Smith, Design of bi-tortuous, anisotropic graphite anodes for fast ion-transport in Li-ion batteries, J. Electrochem. Soc., 162 (2015) A1415-A1423.
[22] B. Suthar, P.W.C. Northrop, D. Rife, V.R. Subramanian, Effect of porosity, thickness and tortuosity on capacity fade of anode, J. Electrochem. Soc., 162 (2015) A1708-A1717.
[23] G.B. Less, J.H. Seo, S. Han, A.M. Sastry, J. Zausch, A. Latz, S. Schmidt, C. Wieser, D. Kehrwald, S. Fell, Micro-scale modeling of Li-ion batteries: parameterization and validation, J. Electrochem. Soc., 159 (2012) A697-A704.
[24] Y.L. Dai, V. Srinivasan, On graded electrode porosity as a design tool for improving the energy density of batteries, J. Electrochem. Soc., 163 (2016) A406-A416.
[25] L. Cai, K. An, Z. Feng, C.D. Liang, S.J. Harris, In-situ observation of inhomogeneous degradation in large format Li-ion cells by neutron diffraction, J. Power Sources, 236 (2013) 163-168.
[26] N. Schulz, R. Hausbrand, L. Dimesso, W. Jaegermann, XPS-surface analysis of SEI layers on Li-Ion cathodes: part I. investigation of initial surface chemistry, J. Electrochem. Soc., 165 (2018) A819-A832.
[27] N. Schulz, R. Hausbrand, L. Dimesso, W. Jaegermann, XPS-surface analysis of SEI layers on Li-Ion cathodes: part II. SEI-composition and formation inside composite electrodes, J. Electrochem. Soc., 165 (2018) A833-A846.
[28] C. Cheng, R. Drummond, S.R. Duncan, P.S. Grant, Micro-scale graded electrodes for improved dynamic and cycling performance of Li-ion batteries, J. Power Sources, 413 (2019) 59-67.
[29] M.S. Whittingham, Ultimate limits to intercalation reactions for lithium batteries, Chem. Rev., 114 (2014) 11414-11443.
[30] S.T. Myung, F. Maglia, K.J. Park, C.S. Yoon, P. Lamp, S.J. Kim, Y.K. Sun, Nickel-rich layered cathode materials for automotive lithium-ion batteries: achievements and perspectives, Acs Energy Lett, 2 (2017) 196-223.

[31] Y.B. Qi, T.J. Jang, V. Ramadesigan, D.T. Schwartz, V.R. Subramanian, Is there a benefit in employing graded electrodes for lithium-ion batteries?, J. Electrochem. Soc., 164 (2017) A3196-A3207.

[32] S.H. Lee, A. Mahadevegowda, C. Huang, J.D. Evans, P.S. Grant, Spray printing of self-assembled porous structures for high power battery electrodes, J. Mater. Chem. A, 6 (2018) 13133-13141.

[33] C. Huang, N.P. Young, P.S. Grant, Spray processing of TiO2 nanoparticle/ionomer coatings on carbon nanotube scaffolds for solid-state supercapacitors, J. Mater. Chem. A, 2 (2014) 11022-11028.

[34] C. Huang, P.S. Grant, One-step spray processing of high power all-solid-state supercapacitors, Sci. Rep., 3 (2013) 2393-1-9.

[35] A.F. Léonard, N. Job, Safe and green Li-ion batteries based on $LiFePO_4$ and $Li_4Ti_5O_{12}$ sprayed as aqueous slurries with xanthan gum as common binder, Materials Today Energy, 12 (2019) 168-178.

[36] X. Xu, C. Qi, Z. Hao, H. Wang, J. Jiu, J. Liu, H. Yan, K. Suganuma, The surface coating of commercial $LiFePO_4$ by utilizing ZIF-8 for high electrochemical performance lithium ion battery, Nano-Micro Lett., 10 (2017) 1-9.

[37] D. Andre, M. Meiler, K. Steiner, C. Wimmer, T. Soczka-Guth, D.U. Sauer, Characterization of high-power lithium-ion batteries by electrochemical impedance spectroscopy. I. Experimental investigation, J. Power Sources, 196 (2011) 5334-5341.

[38] D. Andre, M. Meiler, K. Steiner, H. Walz, T. Soczka-Guth, D.U. Sauer, Characterization of high-power lithium-ion batteries by electrochemical impedance spectroscopy. II: Modelling, J. Power Sources, 196 (2011) 5349-5356.

[39] M.E. Orazem, B. Tribollet, Electrochemical Impedance Spectroscopy, Wiley, New Jersey, 2008.

[40] M. Pathak, M.D. Murbach, C. Pathak, T.J. Jang, Y.B. Qi, D.T. Schwartz, V.R. Subramanian, Fast Impedance Simulation of Lithium-Ion Batteries with Pseudo-Two Dimensional Electrochemical Models, J. Electrochem. Soc., 165 (2018) A1324-A1337.

[41] T. Nordh, in, Uppsala University, 2015.

[42] Y.B. He, M.L. Liu, Z.D. Huang, B. Zhang, Y. Yu, B. Li, F.Y. Kang, J.K. Kim, Effect of solid electrolyte interface (SEI) film on cyclic performance of $Li_4Ti_5O_{12}$ anodes for Li ion batteries, J. Power Sources, 239 (2013) 269-276.

[43] M.G. Verde, L. Baggetto, N. Balke, G.M. Verith, J.K. Seo, Z. Wang, Y.S. Meng, ACS Nano, 10 (2016) 4312-4321.

[44] W. Yang, J. Liu, X. Zhang, L. Chen, Y. Zhou, Z. Zou, Ultrathin $LiFePO_4$ nanosheets self-assembled with reduced graphene oxide applied in high rate lithium ion batteries for energy storage, Appl. Energy, 195 (2017) 1079-1085.

[45] R. Drummond, C. Huang, P.S. Grant, S.R. Duncan, Overcoming diffusion limitations in supercapacitors using layered electrodes, J. Power Sources, 433 (2019) 126579-1-10

[46] R. Drummond, S.R. Duncan, Observer design for the Doyle–Fuller–Newman Li-ion battery model without electrolyte dynamics, J. Energy Storage, 23 (2019) 250-257.

Supplementary Data

Combining composition graded positive and negative electrodes for higher performance Li-ion batteries

Chuan Cheng,[a,b,*] Ross Drummond,[c] Stephen R. Duncan,[c] and Patrick S. Grant[a]

[a]Department of Materials, University of Oxford, Oxford OX1 3PH, UK.

[b]WMG, University of Warwick, Coventry CV4 7AL, UK

[c]Department of Engineering, University of Oxford, Oxford OX1 3PJ, UK.

[*]E-mail: Chuan.Cheng@warwick.ac.uk

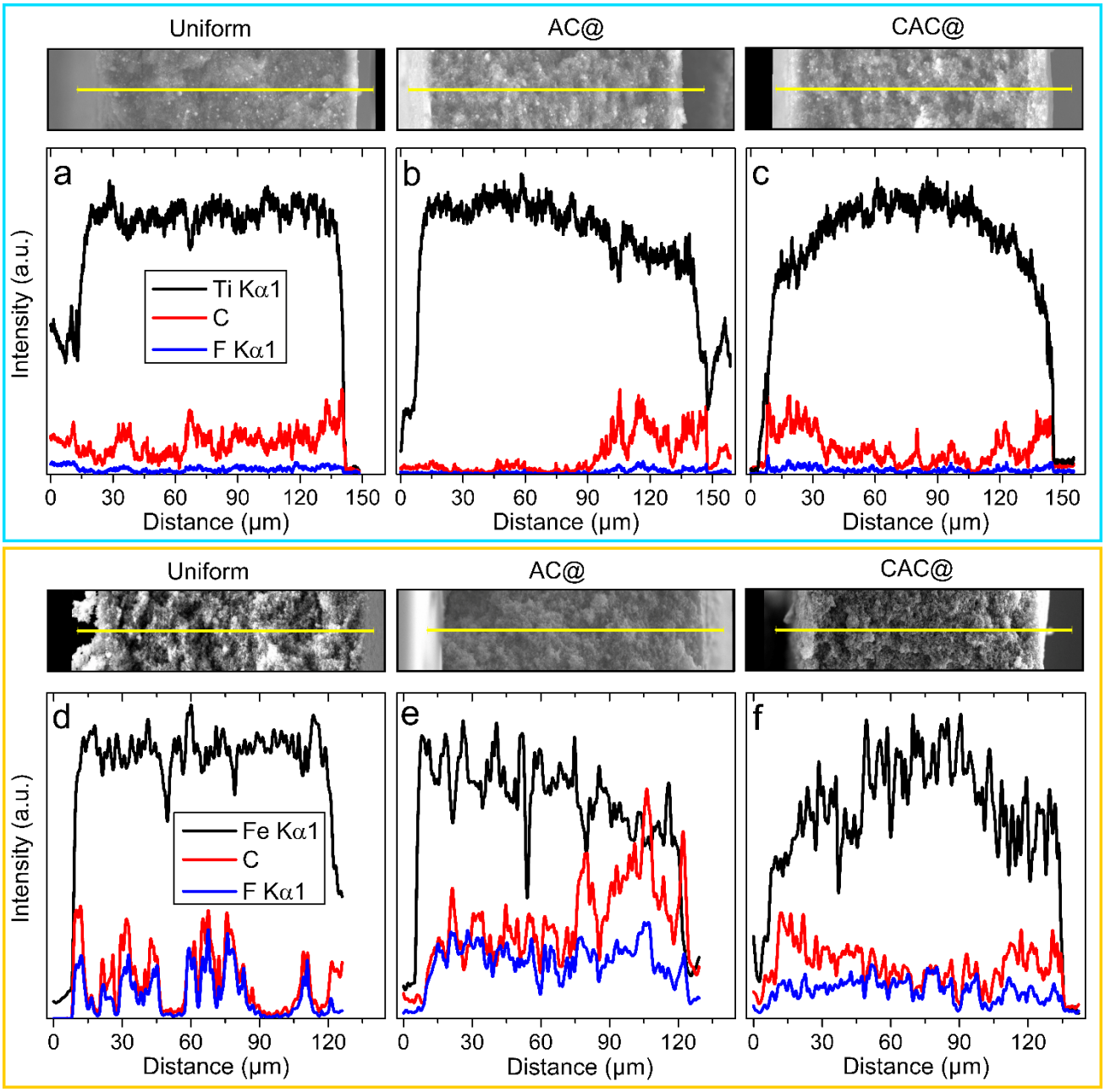

Fig. S1. SEM-EDX element line scans across the thickness of cross-sections (a-c) $Li_4Ti_5O_{12}$ based anodes and (d-f) $LiFeO_4$ based cathodes along the yellow lines in the SEM images shown at the top, with (a, d) uniform, (b, e) AC@ type, and (c, f) CAC@ type materials distribution, where Ti Kα1, Fe Kα1, C, and F Kα1 are attributed to $Li_4Ti_5O_{12}$ active material, $LiFePO_4$ active material, carbon conductive additive, and PVDF binder, respectively. The x-axis distance starts from the electrode surface, and increases towards current collector.

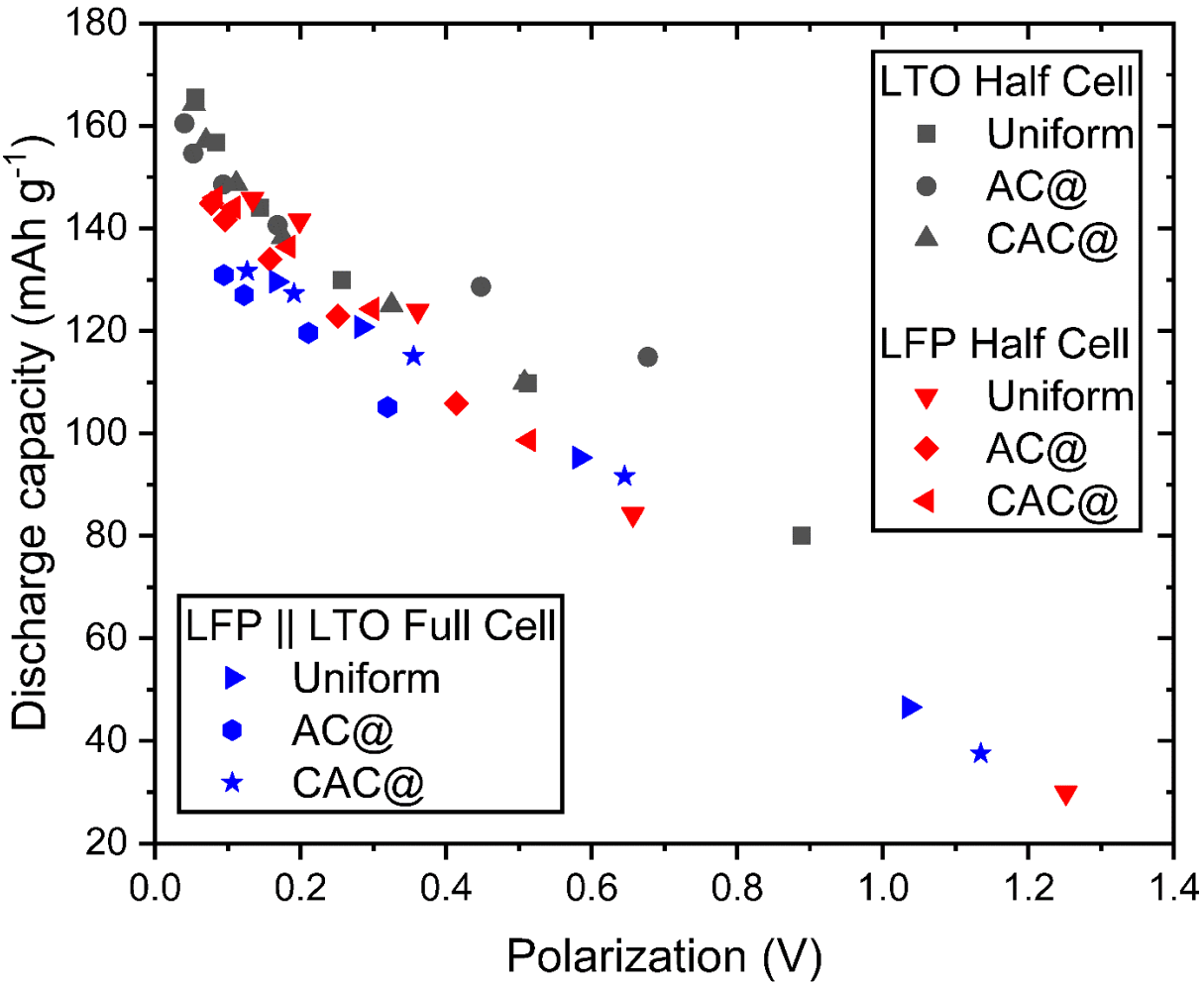

Fig. S2. Discharge capacity across a range of C-rates as a function of polarization for $Li_4Ti_5O_{12}$ (LTO) half-cells, $LiFePO_4$ (LFP) half-cells, and $LiFePO_4$ || $Li_4Ti_5O_{12}$ (LTO||LFP) full cells for uniform and graded electrodes.

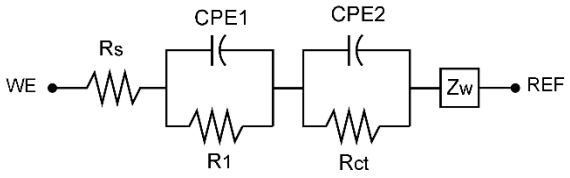

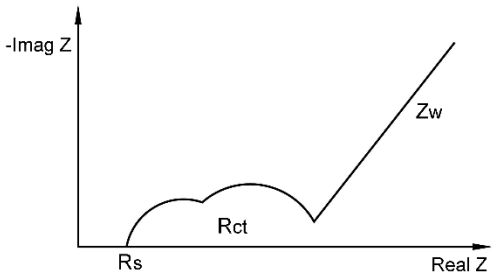

Sample	R_s (Ω)	RC1					RC2					Z_w
		R1 (Ω)	CPE1			τ_1 (s)	R_{ct} (Ω)	CPE2			τ_{ct} (s)	
			Y1 (S $s^{\alpha 1}$)	α1	$C_{eff}1$ (F)			Y2 (S $s^{\alpha 2}$)	α2	$C_{eff}2$ (F)		W (S $s^{1/2}$)
LTO-half, Uniform	4.61	2.49	1.119e-6	0.947	5.47e-7	1.36e-6	9.11	6.13e-4	0.553	9.25e-6	8.43e-5	0.338
LTO-half, AC@	4.53	4.51	1.75e-4	0.936	1.07e-4	4.83e-4	4.94	2.58e-4	0.555	1.23e-6	6.08e-6	0.152
LTO-half, CAC@	4.72	5.15	0.136	0.757	0.121	0.623	8.19	1.27e-3	0.485	9.96e-6	8.16e-5	1.323
LFP-half, Uniform	5.69	3.85e3	7.14e-2	0.857	0.180	693.0	81.0	2.83e-5	0.759	4.11e-6	3.33e-4	4.24e-2
LFP-half, AC@	5.25	1.40e3	1.26e-1	0.958	0.158	221.2	19.5	6.39e-5	0.695	3.40e-6	6.63e-5	9.24e-2
LFP-half, CAC@	4.48	2.87e3	1.21e-1	0.946	0.170	487.9	29.7	8.69e-5	0.637	2.9e-6	8.61e-5	6.83e-2
Full C-rate, Uniform	8.61	2.61e4	7.85e-2	0.874	0.236	6.16e3	173.5	1.60e-5	0.757	2.42e-6	4.20e-4	9.28e-3
Full C-rate, AC@	5.23	4.53e3	1.87e-2	0.918	2.78e-2	1.26e2	21.0	2.48e-5	0.760	2.28e-6	4.79e-5	1.74e-2
Full C-rate, CAC@	5.58	5.95e3	1.09e-2	0.910	1.64e-2	97.6	90.4	1.64e-5	0.783	2.70e-6	2.44e-4	1.24e-2
Full Cycling, Uniform	4.50	1.69e5	1.29e-2	0.717	0.268	4.53e4	147.7	1.70e-5	0.794	3.60e-6	5.31e-4	2.53e-2
Full Cycling, AC@	7.28	1.43e4	1.86e-2	0.857	4.72e-2	6.75e2	106.9	2.32e-5	0.765	3.67e-6	3.92e-4	1.32e-2
Full Cycling, CAC@	5.83	1.80e4	1.02e-2	0.883	2.04e-2	3.67e2	43.9	2.10e-5	0.790	3.28e-6	1.44e-4	1.06e-2

Table S1. Best-fit values of the equivalent circuit corresponding to Nyquist plots shown by the solid lines in Figs. 6a-6d.

R_s and R_{ct} denote cell resistance and transfer resistance, respectively. Impedance for constant phase element (CPE) was $Z_{CPE} = 1/[(j\omega)^{\alpha} Y]$ and the effective capacity of *CPE* was calculated by $C_{eff} = [(1/R)^{(\alpha-1)} Y]^{1/\alpha}$, where $\omega = 2\pi f$ is angular frequency, $0 < \alpha \leq 1$, Y is a constant with unit S s^{α}, and R is resistance. The time constant τ of each RC circuit was $\tau = RC_{eff}$, which represented the time required for charging the capacitor represented by

the effective capacitance of the CPE through resistor *R*. The Warburg impedance for Li ion diffusion is $Z_w = 1/[(j\omega)^{1/2} W]$, where $W = 1/(\sigma\sqrt{2})$ and σ is Warburg coefficient [1]. In the equivalent circuit shown above, the first RC circuit is usually attributed to the impedance at the active particle surface and the second RC circuit usually attributed to the charge transfer of faradaic reactions [2-5].

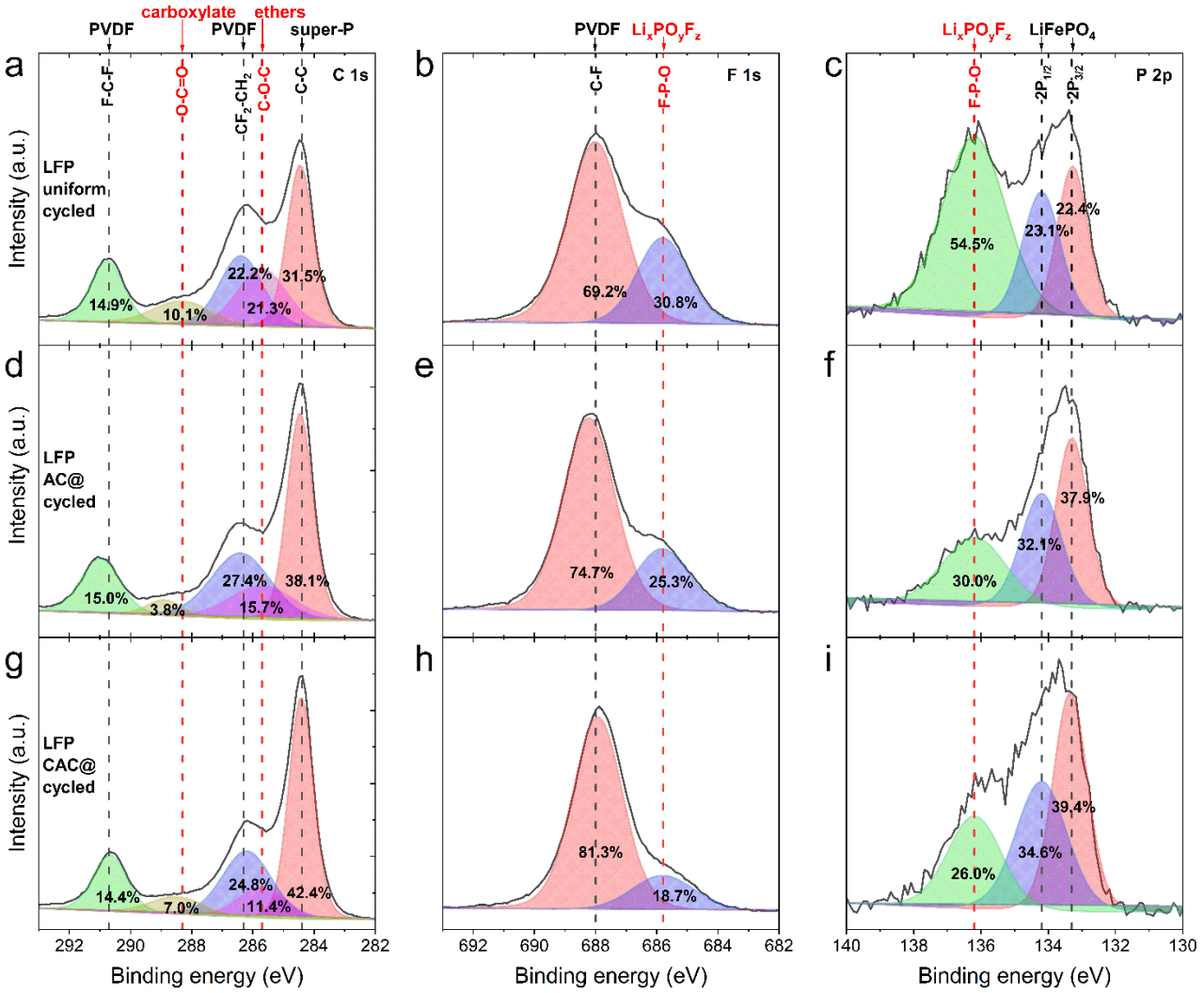

Fig. S3. X-ray photoelectron spectra (XPS) analysis of the $LiFePO_4$-based cathodes recovered from full-cells after 200 cycles at 1C in Fig. 3f. (a-c) cycled uniform cathode, (d-f) cycled AC@ graded cathode, and (g-i) cycled CAC@ graded anode. (a, d, g) C 1s spectra, (b, e, h) F 1s spectra, and (c, f, i) P 1s spectra. The vertical dashed lines indicate the labelled reference chemical bonds taken from the literature [6-10]. The estimated atomic ratio of C, F and P obtained by peak deconvolution and integration (filled regions) is noted on the plots.

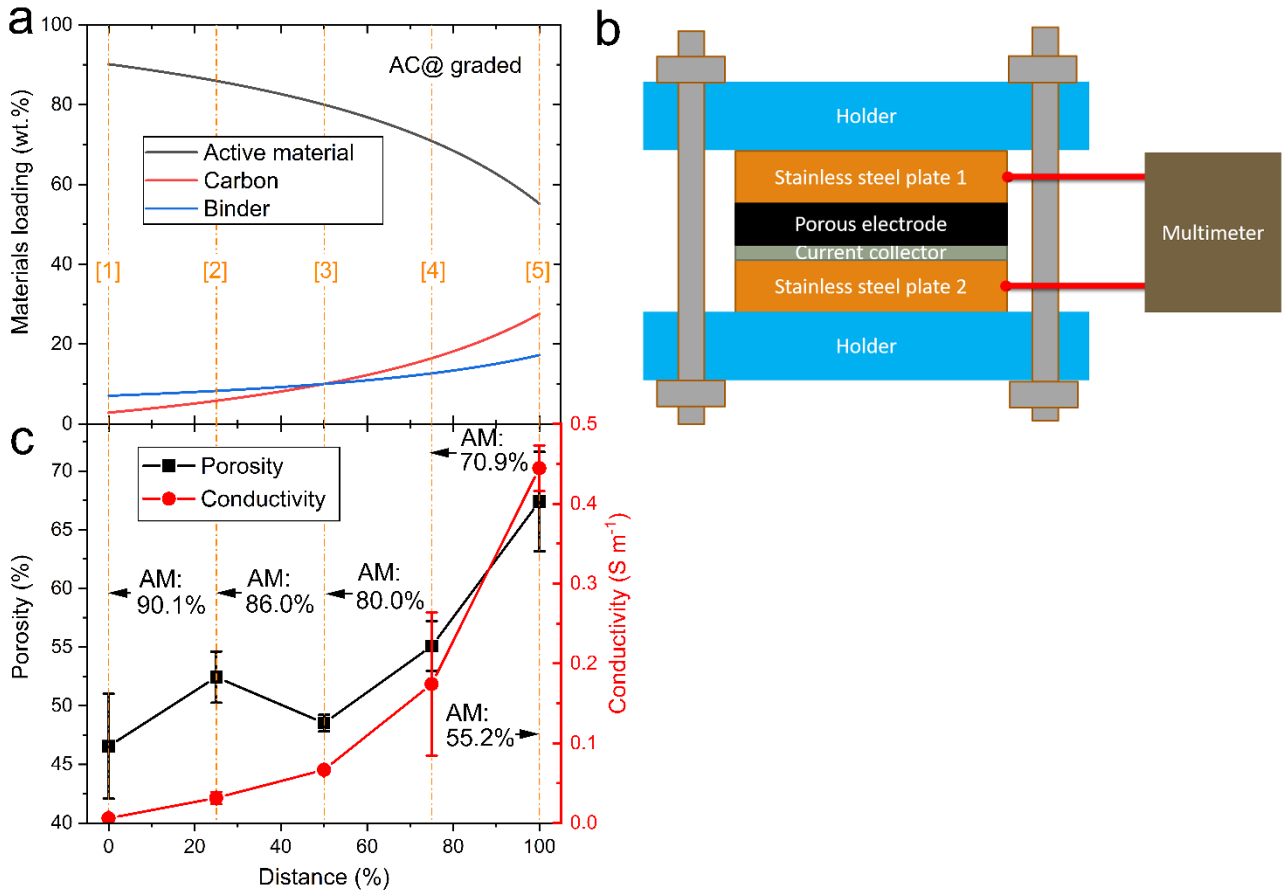

Fig. S4. (a) Schematic diagram of the intended AC@ type materials distribution across the thickness of the electrode, which is the same as Fig. 1c in the main text. Distance refers to the distance from the surface of the electrode (i.e. at the electrode/separator interface), increasing towards the current collector. From (a), five discrete composition ratios of active material (**AM**, LFP-based): carbon: binder are selected, denoted as [1] to [5]. Five uniform electrodes with these composition ratios were fabricated by the same spraying deposition process. After a similar extent of calendaring, the porosity and the electronic conductivity were measured. (b) Illustration of the apparatus for the non-destructive measurement of electronic conductivity of the uniform electrode. (c) The variation of uniform electrode porosity (left) and electronic conductivity (right) as a function of composition, related to five discrete positions through the AC@ graded electrode.

In order to investigate effects of compositional change on the local porosity and electronic conductivity through the electrode thickness, a series of composition ratios corresponding to different distances (or depth) through a graded electrode, as denoted by [1] to [5] in Fig. S4a were selected. Uniform electrodes of these compositions

were then fabricated and their average porosity and electronic conductivity measured. The porosity of the uniform electrode was measured according to:

$$Porosity = \left[1 - \rho_{electrode} \times \left(\frac{M_{AM}}{\rho_{AM}} + \frac{M_{Binder}}{\rho_{Binder}} + \frac{M_{Carbon}}{\rho_{Carbon}}\right)\right] \times 100\%$$

where ρ represents density (units: g/cm^3) and M represents the weight fraction (unit: wt.%). The electronic conductivity σ of the uniform electrodes was measured using the experimental apparatus shown schematically in Fig. S4b and according to:

$$\sigma = \frac{l}{(R - R_{Al})A}$$

where l is the thickness of the electrode, A is the surface area of the electrode pressed in between two stainless steel plates, R is the resistance measured by the multimeter, and R_{Al} is the resistance of the Al foil without the electrode coating.

Fig. S4c shows that both porosity and conductivity increased with increased carbon fraction (and therefore decreasing active material fraction).

References

[1] J. Bisquert, G. Garcia-Belmonte, P. Bueno, E. Longo, L.O.S. Bullhoes, Impedance of constant phase element (CPE)-blocked diffusion in film electrodes, J. Electroanal. Chem., 451 (1998) 229-234.

[2] D. Andre, M. Meiler, K. Steiner, H. Walz, T. Soczka-Guth, D.U. Sauer, Characterization of high-power lithium-ion batteries by electrochemical impedance spectroscopy. II: Modelling, J. Power Sources, 196 (2011) 5349-5356.

[3] D. Andre, M. Meiler, K. Steiner, C. Wimmer, T. Soczka-Guth, D.U. Sauer, Characterization of high-power lithium-ion batteries by electrochemical impedance spectroscopy. I. Experimental investigation, J. Power Sources, 196 (2011) 5334-5341.

[4] I.D. Raistrick, D.R. Franceschetti, J.R. Macdonald, Theory, in: E. Barsoukov, J.R. Macdonald (Eds.) Impedance Spectroscopy Theory, Experiment, and Applications, John Wiley & Sons, Inc., New Jersey, 2005.

[5] M.E. Orazem, B. Tribollet, Electrochemical Impedance Spectroscopy, Wiley, New Jersey, 2008.

[6] T. Nordh, in, Uppsala University, 2015.

[7] Y.B. He, M.L. Liu, Z.D. Huang, B. Zhang, Y. Yu, B. Li, F.Y. Kang, J.K. Kim, Effect of solid electrolyte interface (SEI) film on cyclic performance of $Li_4Ti_5O_{12}$ anodes for Li ion batteries, J. Power Sources, 239 (2013) 269-276.

[8] M.G. Verde, L. Baggetto, N. Balke, G.M. Verith, J.K. Seo, Z. Wang, Y.S. Meng, ACS Nano, 10 (2016) 4312-4321.

[9] N. Schulz, R. Hausbrand, L. Dimesso, W. Jaegermann, XPS-surface analysis of SEI layers on Li-Ion cathodes: part II. SEI-composition and formation inside composite electrodes, J. Electrochem. Soc., 165 (2018) A833-A846.

[10] N. Schulz, R. Hausbrand, L. Dimesso, W. Jaegermann, XPS-surface analysis of SEI layers on Li-Ion cathodes: part I. investigation of initial surface chemistry, J. Electrochem. Soc., 165 (2018) A819-A832.